

See discussions, stats, and author profiles for this publication at: <https://www.researchgate.net/publication/233895690>

Evaporation and Marangoni Driven Convection in Small Heated Water Droplets

ARTICLE in LANGMUIR · MAY 2009

Impact Factor: 4.46 · DOI: 10.1021/la061572l

CITATIONS

74

READS

141

5 AUTHORS, INCLUDING:



Fabien Girard

Aix-Marseille Université

9 PUBLICATIONS 302 CITATIONS

SEE PROFILE



Sylvain Faure

Atomic Energy and Alternative Energies Com...

20 PUBLICATIONS 277 CITATIONS

SEE PROFILE



Annie Steichen

Aix-Marseille Université

81 PUBLICATIONS 521 CITATIONS

SEE PROFILE



Mickaël Antoni

Aix-Marseille Université

8 PUBLICATIONS 229 CITATIONS

SEE PROFILE

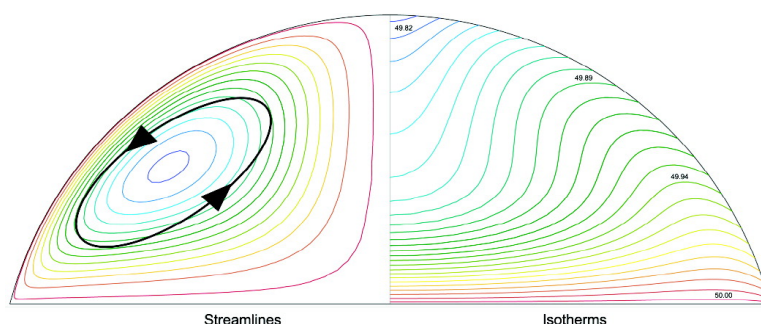
Research Article

Evaporation and Marangoni Driven Convection in Small Heated Water Droplets

Fabien Girard, Mickal Antoni, Sylvain Faure, and Annie Steinchen

Langmuir, **2006**, 22 (26), 11085-11091 • DOI: 10.1021/la061572l • Publication Date (Web): 24 November 2006

Downloaded from <http://pubs.acs.org> on May 1, 2009



More About This Article

Additional resources and features associated with this article are available within the HTML version:

- Supporting Information
- Links to the 5 articles that cite this article, as of the time of this article download
- Access to high resolution figures
- Links to articles and content related to this article
- Copyright permission to reproduce figures and/or text from this article

[View the Full Text HTML](#)

Evaporation and Marangoni Driven Convection in Small Heated Water Droplets

Fabien Girard,[†] Mickaël Antoni,^{*,†} Sylvain Faure,[‡] and Annie Steinchen^{*,†}

Thermodynamique et modélisation des milieux hors d'équilibre, UMR-CNRS 6171, Université Paul Cézanne—Aix-Marseille III, BP 451 Avenue Escadrille Normandie-Niemen, 13397 Marseille Cedex 20, France, and CEA—Marcoule Laboratoire des procédés avancés de décontamination DTCD/SPDE/LPAD, 30207 Bagnols-sur-Cèze Cedex, France

Received June 1, 2006. In Final Form: September 5, 2006

Evaporation dynamics of small sessile water droplets under microgravity conditions is investigated numerically. The water–air interface is free, and the surrounding air is assumed to be quasisteady. The droplet is described by Navier–Stokes and heat equations and its surrounding water/air gaseous phase with Laplace equation. In the thermodynamic conditions of the simulations presented herein, the evaporative mass flow is nonlinear. It shows a minimum that indicates the existence of qualitative changes in the evaporative regimes although the droplet is sessile. Due to temperature gradients on the free interface, Marangoni motion occurs and generates inside the droplet convection cells that furthermore exhibit small fluctuating motion as evaporation goes on.

1. Introduction

Evaporation of a liquid droplet is unavoidable unless the surrounding gaseous phase of this droplet is saturated with the vapor of the liquid. In this very peculiar situation, liquid/vapor equilibrium is characterized by mass flows from liquid to vapor and from vapor to liquid that exactly compensate. When this balance is in the favor of the vapor phase, evaporation takes place. The understanding of vapor flow at equilibrium is of fundamental interest and remains yet unresolved for true sessile drop equilibrium even in a saturated vapor. Still, in recent years important studies of evaporating liquid droplets on heating substrates have been carried out to investigate the dynamics generated by the outgoing matter flow. It is now well-established that pinned drying droplets containing suspensions (coffee, microspheres, and pigments, etc) yield segregation patterns rather than a uniform final deposit after complete evaporation of the fluid.^{1–10} But the full understanding of evaporation phenomena and explanation of pattern formation are still open questions that nowadays motivate important scientific activity both for fundamental and applied purposes. The control of drying systems containing microparticles is for example of first importance for applications in the paint industry to prevent segregation phenomena of the pigments that would lead to the formation of unwanted sticky patterns. Evaporation understanding also appears to be determinant for the manufacture of new materials,^{11,12} for

the creation of a microwell on soluble polymer substrate,⁵ or to explain the starburst pattern appearing when DNA is deposited from evaporating droplets.¹³

The explanation of the existence of such nonuniform patterns after droplet evaporation still requires further investigations even in the simplified situation of axi-symmetric pinned droplets. In the original work of Deegan,^{1,2} the existence of circular patterns is related to the large outgoing flow of solvent at the droplet three phases contact line. This flow carries the microparticles from the axis of the droplet to its contact line, where microparticles finally progressively accumulate and reinforce the pinning of the droplet if adsorption strength is sufficient. A similar approach is used to explain the formation of connected polygons formed by Marangoni–Bénard flow in aqueous sessile droplets containing both surfactants and microspheres.^{8,14} In many studies, heat conduction is assumed to be the dominant mode of thermal energy transport in small droplets. Still, several experiments show that convection can occur even for small droplets.^{6,15–18} Moreover, recent experimental results³ indicate that particle deposition in octane droplets can be localized predominantly at the center of the droplet instead of at the contact line. The explanation of this phenomenon is linked to the temperature gradient between the apex and the contact line of the droplet that generates a nonuniform surface tension on the interface. Marangoni instability then enters into play and generates surface hydrodynamic motions.^{19–21} Because the basis of the droplet is warmer, surface tension is smaller and hence drives out the fluid to the top of the interface that is cooler and where surface tension is larger. Due to viscous

* To whom correspondence should be addressed: m.antoni@univ-cezanne.fr.

[†] Université Paul CÉZANNE.

[‡] CEA—Cedex, France.

(1) Deegan, R. D.; Bakajin, O.; Dupont, T. F.; Huber, G.; Nagel, S. R.; Witten, T. A. *Nature* **1997**, *389*, 827–829.

(2) Deegan, R. D.; Bakajin, O.; Dupont, T. F.; Huber, G.; Nagel, S. R.; Witten, T. A. *Phys. Rev. E* **2000**, *62*, 756–765.

(3) Hu, H.; Larson, R. G. *J. Phys. Chem. B* **2006**, *110*, 7090–7094.

(4) Fischer, B. J. *Langmuir* **2002**, *18*, 60–67.

(5) Gonuguntla, M.; Sharma, A. *Langmuir* **2004**, *20*, 3456–3463.

(6) Mougin, K.; Haidara, H. *Langmuir* **2002**, *18*, 9566–9569.

(7) Sommer, A. P.; Ben-Moshe, M.; Magdassi, S. *J. Phys. Chem. B* **2004**, *108*, 8–10.

(8) Truskett, V. N.; Stebe, K. J. *Langmuir* **2003**, *19*, 8271–8279.

(9) Lin, Z.; Granick, S. *J. Am. Chem. Soc.* **2005**, *127*, 2816–2817.

(10) Popov, Y. O.; Witten, T. A. *Phys. Rev. E* **2003**, *68*, 036306.

(11) Kawase, T.; Siringhuas, H.; Friend, R. H.; Shimoda, T. *Adv. Mater.* **2001**, *13*, 1601.

(12) Norris, D. J.; Arlinghaus, E. G.; Meng, L. L.; Heiny, R.; Scriven, L. E. *Adv. Mater.* **2004**, *16*, 1393.

(13) Jing, J.; Reed, J.; Huang, J.; Hu, X.; Clarke, V.; Edington, J.; Housman, D.; Anantharaman, T. S.; Huff, E. J.; Mishra, B.; Porter, B.; Shenker, A.; Wolfson, E.; Hiort, C.; Kantor, R.; Aston, C. *Proc. Natl. Acad. Sci. U.S.A.* **1998**, *95*, 8046.

(14) Popov, Y. O. *Phys. Rev. E* **2005**, *71*, 036313.

(15) Bonacina, C.; Del Giudice, S.; Comini, G. *J. Heat Transfer* **1979**, *101*, 441–446.

(16) Grandas, L. Doctoral thesis, Université Paul Cézanne, Marseille, France, 2004.

(17) Lorenz, J.; Mickic, B. B. *J. Heat Transfer* **1970**, *92*, 46–52.

(18) Zhang, Y.; McLaughlin, J. B.; Finch, J. A. *Chem. Eng. Sci.* **2001**, *56*, 6605–6616.

(19) Ruiz, O. E.; Black, W. Z. *J. Heat Transfer* **2002**, *124*, 854–863.

(20) Hu, H.; Larson, R. G. *Langmuir* **2005**, *21*, 3972–3980.

(21) Ozen, O.; Narayanan, R. *Ind. Eng. Chem. Res.* **2005**, *44*, 1342–1348.

Table 1. Data Used for the Simulations Presented Herein

T_s	°C	30	40	50	60	70
R	m	1.00×10^{-3}	1.00×10^{-3}	1.00×10^{-3}	1.00×10^{-3}	1.00×10^{-3}
H	%	20	20	20	20	20
T	°C	20	20	20	20	20
s	10^{-3} N/m	71.45	69.66	67.87	66.08	64.29
C_v	$\text{m}^2/(\text{s}^2 \cdot \text{K})$	4180	4176	4176	4179	4186
k	$\text{kg} \cdot \text{m}/(\text{s}^3 \cdot \text{K})$	6.10×10^{-1}	6.22×10^{-1}	6.33×10^{-1}	6.45×10^{-1}	6.57×10^{-1}
m	$\text{kg}/(\text{m} \cdot \text{s})$	7.98×10^{-4}	6.54×10^{-4}	5.47×10^{-4}	4.66×10^{-4}	4.04×10^{-4}
ρ_0	kg/m^3	993.96	991.29	988.55	985.75	982.86
$\kappa = k/(\rho C_v)$	m^2/s	1.47×10^{-7}	1.50×10^{-7}	1.53×10^{-7}	1.57×10^{-7}	1.60×10^{-7}
$\nu = \mu/\rho_0$	m^2/s	8.03×10^{-7}	6.59×10^{-7}	5.53×10^{-7}	4.73×10^{-7}	4.11×10^{-7}
$U = Ca\sigma/\mu$	m/s	6.26	9.93	14.46	19.82	25.94
$Ca = 1 - \sigma(T)/\sigma(1^\circ\text{C})$		6.99×10^{-2}	9.32×10^{-2}	1.17×10^{-1}	1.40×10^{-1}	1.63×10^{-1}
$Re = UL/\nu$		7796	15065	26137	41905	63047
$Pr = \nu/\kappa$		5.46	4.39	3.61	3.02	2.58
ΔH_{vap}	J/mol	43689	43318	42935	42538	42127

forces, interface Marangoni motion then drags the adjacent fluid layers to the top of the droplet and yields convective motions inside the droplet. As a result, when a droplet contains microparticles, these microparticles are periodically carried by convection from the substrate to the droplet interface and back to the substrate and can hence accumulate at its center.

In the present paper we investigate numerically the evaporating dynamics of a pure water axi-symmetric sessile droplet on a horizontal heating substrate. Beside the description of evaporation time and time-dependent mass flow, we also propose to focus on the role of free interface phenomena with the aim of obtaining a quantitative description of Marangoni driven convection inside the droplet. We restrict in the following the investigations to the droplet evaporating regime where the contact line radius R remains constant but where its contact angle θ decreases.²² Depending on the heating substrate constitution, this regime can prevail for the evaporation of more than 80% of the initial volume of water droplets^{23,24} and hence persists long enough for convection phenomena to be relevant. The droplets we consider in this article are supposed to be small enough for buoyancy effects to be negligible.²⁵ Furthermore, besides assuming droplets to be sessile, we also suppose that they keep a spherical cap geometry for the duration of the simulations.^{18,24,26} We finally assume that the substrate is ideal in the sense that it is characterized by an infinite thermal conductivity and that its size is exactly the size of the base of the droplet. The solid–liquid boundary can, in these conditions, be treated as isothermal. This last approximation is justified for metallic substrates where droplets remain sessile up to contact angles that can take values smaller than 10° .^{27,28} We report in the following mainly about the results obtained for droplets with radius $R = 1$ mm, far-field temperature $T_\infty = 20$ °C, and relative humidity $H = 20\%$. Hence, the unique parameter is the substrate temperature T_s that will range between $T_s = 30$ °C and $T_s = 70$ °C. The detailed values of the data used in the simulations are given in Table 1.

2. Approximations and Numerical Method

For small droplets, hydrostatic pressure is negligible when compared to surface tension effects. For contact angle θ , the balance between the two phenomena is given by the ratio between maximal hydrostatic pressure in the droplet $P_H = \rho g R(1 - \cos(\theta))/\sin(\theta)$ and

Laplace pressure $P_L = 2\sigma \sin(\theta)/R$ that yields for millimetric water droplet under the thermodynamic conditions of our study $P_L/P_H = 2\sigma \sin^2(\theta)/(\rho g R^2(1 - \cos(\theta)))$. For $R = 1$ mm and $\theta < 90^\circ$, $P_L/P_H > 10$. Hence, for such small droplets, surface effects prevail and govern the droplet properties.

When investigating the problem of small evaporating water droplets, temperature differences inside the droplet are smaller than 1 °C. This allows the use of Boussinesq approximation assuming the fluid in the considered system has constant properties. Heat capacity c_v , viscosity μ , density ρ , and thermal diffusivity k are hence assumed to be constant in the droplet. For many systems these quantities vary by less than 1% for temperature changes larger than 10 °C. We can hence neglect buoyancy effects inside the droplet. Another way to evaluate the relative strength of the buoyancy-induced flow compared to Marangoni flow is to consider the dimensionless number $B = \rho g h^2 C / (7.1375 b)$.^{20,29} With values $\rho = 10^3$ kg/m³, $g = 9.81$ m/s², $h = 10^{-3}$ m, $\beta = 0.1790 \times 10^{-3}$ N·m⁻¹·K⁻¹, and $C = 2.07 \times 10^{-4}$, one gets $B \approx 2 \times 10^{-3}$ showing that buoyancy induced flow is weak compared to Marangoni driven flow.

In these conditions the Navier–Stokes and heat equation reduce to differential equations involving Reynolds and Prandtl numbers that are given as $Re = UR/\nu$ and $Pr = \nu/\kappa$ with $\nu = \mu/\rho$ the kinetic viscosity of water and $\kappa = k/(\rho c_v)$ its thermal conductivity. When neglecting gravitation and hydrostatic pressure gradients, the Navier–Stokes equation for axi-symmetric systems is then written as

$$u_r \frac{\partial u_r}{\partial r} + u_z \frac{\partial u_r}{\partial z} = \frac{1}{Re} \left(\frac{1}{r} \frac{\partial}{\partial r} \left(r \frac{\partial u_r}{\partial r} \right) - \frac{u_r}{r^2} + \frac{\partial^2 u_r}{\partial z^2} \right) \quad (1)$$

$$u_r \frac{\partial u_z}{\partial r} + u_z \frac{\partial u_z}{\partial z} = \frac{1}{Re} \left(\frac{1}{r} \frac{\partial}{\partial r} \left(r \frac{\partial u_z}{\partial r} \right) + \frac{\partial^2 u_z}{\partial z^2} \right) \quad (2)$$

where r and z are the normalized nondimensional cylindrical coordinates ($r \rightarrow r/R$ and $z \rightarrow z/R$) and u_r (respectively u_z) the radial (respectively axial) normalized component of the velocity at point (r, z) (i.e., $u_z \rightarrow u_z/U$ and $u_r \rightarrow u_r/U$, where typical velocity U is defined below). The corresponding heat equation is written as

$$u_r \frac{\partial T}{\partial r} + u_z \frac{\partial T}{\partial z} = \frac{1}{RePr} \left(\frac{1}{r} \frac{\partial}{\partial r} \left(r \frac{\partial T}{\partial r} \right) + \frac{\partial^2 T}{\partial z^2} \right) \quad (3)$$

where viscous dissipative terms are omitted. Finally the continuity equation inside the droplet is written as

$$\frac{1}{r} \frac{\partial(r u_r)}{\partial r} + \frac{\partial u_z}{\partial z} = 0 \quad (4)$$

All quantities of the problem, but the typical velocity U , are known. This velocity is determined by the Marangoni velocity flow on the free interface of the droplet. One straightforward way to define U for such systems is to use the capillary number $Ca(T) = \mu(T_s) U(T_s)/$

(22) Bourges-Monnier, C.; Shanahan, M. E. *R. Langmuir* **1995**, *11*, 2820–2829.

(23) Hu, H.; Larson, R. G. *J. Phys. Chem. B* **2002**, *106*, 1334–1344.

(24) Rymkiewicz, J.; Zbigniew, Z. *Int. Commun. Heat Mass Transfer* **1993**, *20*, 687–697.

(25) De Gennes, P. G.; Brochard Wyart, F.; Quéré, D. *Gouttes, bulles, perles et ondes*; Belin: Paris, 2000.

(26) Sefiane, K.; Tadriss, L.; Douglas, M. *Int. J. Heat Mass Transfer* **2003**, *46*, 4527–4534.

(27) Erbil, H. Y.; Dogan, M. *Langmuir* **2000**, *16*, 9267–9273.

(28) Erbil, H. Y.; Meric, R. A. *J. Phys. Chem. B* **1997**, *101*, 6867–6873.

(29) Pearson, J. R. A. *J. Fluid Mech.* **1958**, *4*, 489–500.

$\sigma(T)$, where μ is the viscosity and U the typical velocity at temperature T_s and where $\sigma(T)$ is the surface tension of liquid water at any temperature T . The capillary number is a nondimensional number that expresses the relative importance of viscosity and capillary forces that can also be defined by $Ca(T) = 1 - \sigma(T)/\sigma(T_0)$, where $\sigma(T_0)$ is the surface tension at reference temperature $T_0 = 1^\circ\text{C}$. We assume furthermore that the surface tension is given by equation of state $\sigma(T) = \sigma(T_0) - \beta(T - T_0)$, where $\beta = 0.1790 \text{ N}\cdot\text{m}^{-1}\cdot\text{K}^{-1}$ is a positive constant characteristic of water. The value of the velocity $U(T_s)$ is finally obtained from the two previous expressions of the capillary number. It is given in Table 1 for the simulations of this article.

The boundary conditions of the droplet at the heating substrate contact region are characterized by equal temperature T_s and zero velocity field (i.e., no slip condition and no fluid flow across the boundary). Moreover, as the droplet is assumed to be axis-symmetric for all time, the radial velocity components and the radial gradient of temperature are zero on the symmetry axis. Hence boundary conditions at the substrate level are written as

$$u_r(r,0) = 0, u_z(r,0) = 0, T(r,0) = T_s \quad (5)$$

while on the droplet symmetry axis we have

$$u_r(0,z) = 0, \quad \frac{\partial u_z}{\partial r}\bigg|_{(0,z)} = 0, \quad \frac{\partial T}{\partial r}\bigg|_{(0,z)} = 0 \quad (6)$$

We assumed previously that the droplet keeps a spherical cap geometry as evaporation goes on. Hence, there is no local interface deformation of the free boundary induced for instance by an inward motion due to outward mass flow. Velocities on the free interface are hence tangential and point functions are as expected from thermocapillary convection. The interface temperature then results from a balance between thermocapillary convection and heat diffusion across the water droplet.

The boundary conditions for the gaseous phase rely on the diffusive properties of vapor in air. In principle the limiting step of the evaporation rate could be either the mass-transfer rate across the free interface or the diffusive mechanism of the molecules in the vicinity of the droplet. The transfer rate across the interface is a molecular process that has typical time 10^{-10} s , whereas diffusion of molecules in air has a typical time $R^2/D \approx 10^{-5} \text{ s}$, where $D = 0.2443 \text{ cm}^2\cdot\text{s}^{-1}$ is the diffusion coefficient of vapor in air. These rough estimations indicate that time scales are different by 5 orders of magnitude.¹⁴ This is indeed the case in many experiments and moreover justified by the fact that evaporative processes of small droplets range usually between a few seconds and a few minutes.³⁰ This is far long enough for the droplet surrounding gaseous phase to reach its equilibrium. Practically experiments show that the time required for air to reach a stationary state in the vicinity of the droplet is about 0.04 s for a 1 mm radius droplet.^{1,2,23} Equilibrium outside the droplet is hence rapidly achieved, and we can reasonably assume in the following that diffusion in air is a quasisteady process. As a result, the vapor concentration field is ruled by Laplace equation. But, in this work, the substrate temperature T_s ranges between 30 and 70 $^\circ\text{C}$, while the far-field temperature T_∞ is fixed to 20 $^\circ\text{C}$. Hence, both concentration gradients and temperature gradients should be simultaneously considered, and the gaseous phase should be treated as a mixture of vapor and air. Because the temperature difference between substrate and far field is larger than 10 $^\circ\text{C}$, temperature gradients prevail and rule the evaporative dynamics of the droplet. Still, as for the vapor concentration, thermal equilibrium in the gaseous phase is reached fast enough to assume heat diffusion to be a quasisteady process when compared to droplet volume characteristic evolution time. Laplace equation for the temperature $\Delta T = 0$ is then sufficient to achieve a reliable description of the temperature profile in the gaseous phase.

Boundary conditions are here determined by the vapor concentration in the far field (i.e. in this paper a computational boundary at distance $160R$ from the center of the droplet) and in the neighborhood of the droplet. The first are given by T_∞ and the relative humidity

H , whereas the second are fixed by the temperature and the water saturated vapor concentration in the vicinity of the droplet free interface. The latter is obtained from the local temperature on the droplet free interface that is deduced from the resolution of eqs 1–4 for the droplet. The water concentration in air is then straightforwardly deduced from its partial pressure, assuming that the pressure of air is set to 1 atm everywhere. Under these conditions, the evaporative mass flow is ruled by the free interface temperature and the vapor concentration far apart from the droplet.

To seek solutions for Laplace, Navier–Stokes, and heat equations, we use the finite element method calculation facilities proposed by FIDAP 8.7.2. The mesh grid elements used for the droplet are refined at both the contact line and free interface levels to improve the simulation precision and avoid convergence problems. The droplet is initially supposed to be at the temperature of the substrate. Liquid water and air are treated successively, and the coupling between both is determined through a linear interpolation of the interface temperature values for the mesh grid of air and droplet. This procedure is iterated up until the droplet is evaporated. Practically, this goal is not completely achieved since, due to stability problems, simulations are usually stopped for contact angles close to 10° .

A campaign of test simulations were devoted to determine adapted meshing and to make numerical outputs independent of the used mesh grid. We used a paved meshing that is superior for arbitrary geometries when compared to mapped mesh (i.e., rectangular computational domains). Paved meshes allow a transition from coarse to very fine elements in a short distance. The paved mesh we use is refined at the triple line level and at the apex of the droplet. The sizes of the elements follow a geometric law, and the numbering of all the nodes is optimized to save CPU time. At the bottom and the free interface boundaries more than 100 nodes are used, and at the droplet edge the distance between two successive nodes of the meshing is smaller than $R/300$, where R is the radius of the droplet. In the gaseous phase, we use typically 20 000 mesh nodes. For the droplet, the number of elements depend on the contact angle, and we typically use 3000 elements when $\theta \approx 80^\circ$ and 2000 when $\theta < 15^\circ$. Tests were performed with up to 10 000 mesh elements, but, regarding the precision requirements and the convergence strategy mentioned next, no significant differences were observed in the calculation outputs.

The resolution of nondimensional Laplace, heat, and Navier–Stokes equations with the previously discussed droplet boundary conditions determines the outgoing heat flow for each interface element. This allows in particular the computation of the value of the dimensionless total outgoing heat flow ϕ that is defined as the integrated flux along the droplet free surface. It is computed from the dimensionless normal temperature gradients in the gaseous phase. The actual heat flow finally is written as

$$\frac{dQ}{dt} = -DR(c(T_s) - Hc(T_\infty))\Delta H_{\text{vap}}(T_s)\phi \quad (7)$$

where $\Delta H_{\text{vap}}(T_s)$ is the latent heat of vaporization of water at temperature T_s , where $c(T_s)$ (respectively $c(T_\infty)$) is the saturated vapor concentration of water at temperature T_s (respectively T_∞), and where D and H were defined previously. Concentration $c(T)$ on the interface is computed assuming the vapor is a perfect gas³¹ and from the value of the air saturated vapor pressure of water.³² The heat flow ϕ depends on the droplet contact angle, that itself evolves in time due to evaporation. Nontrivial time dependence in eq 7 is hence coming from the evolution of ϕ .

The total droplet evaporative mass loss over the surface of the drop is then determined by the equation

$$\frac{dm}{dt} = -DR(c(T_s) - Hc(T_\infty))\phi \quad (8)$$

(31) Margerit, J.; Sero-guillaume, O. *Int. J. Heat Mass Transfer* **1996**, 39 (18), 3887–3898.

(32) Perry, R. H.; Green, D. W.; Maloney, J. O. *Perry's Chemical Engineers' Handbook*; McGraw-Hill: New York, 1997.

(30) Shanahan, M. E. R. *Langmuir* **2002**, 18, 7763–7765.

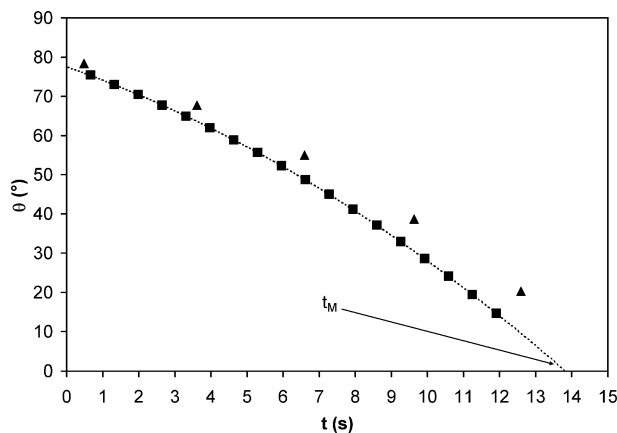


Figure 1. Time evolution of the contact angle for $T_s = 60\text{ }^{\circ}\text{C}$, $T_{\infty} = 26\text{ }^{\circ}\text{C}$, $H = 40\%$, and $R = 0.515\text{ mm}$. Squares correspond to numerical outputs, and the dashed line is obtained from a quadratic power law interpolation of these data. t_M is the estimated total evaporation time. Triangles are obtained from experiments of ref 33.

This equation is solved to obtain the mass $m(t + \Delta t)$ of the droplet at iteration time $t + \Delta t$ from its mass $m(t)$ at time t . The new height of the droplet is then computed before eqs 1–4 to be resolved for the next time step. This procedure is iterated from initial condition $\theta \approx 80^{\circ}$ down to contact angle $\theta \approx 10^{\circ}$ beyond which convergence of numerical calculations becomes critical. In all the simulations we have set $\Delta t/t_M < 10^{-2}$, where t_M is the maximal evaporation time defined below.

The convergence strategy followed in the simulations consists of first computing temperatures down to a rough intermediate precision. Velocities are then calculated also down to a similar precision. This convergence procedure is repeated decreasing at each converge step the precision requirements by 1 order of magnitude down to relative error in dimensionless temperatures (respectively velocities) smaller than 10^{-6} (respectively 10^{-4}).

3. Discussion

The total droplet evaporation time t_M is obtained from the time evolution of the contact angle $\theta(t)$. Its evolution is displayed in Figure 1 together with the evaporation time estimated using a quadratic power law interpolation of $\theta(t)$ down to $\theta(t) = 0^{\circ}$. For most of the simulations, the runs are stopped at $\theta \approx 10^{\circ}$ since for smaller angles important instabilities appear in the computation. They are due to either insufficient mesh grid precision or to the appearance of bifurcations in the hydrodynamics of the droplet that cannot be resolved with the convergence requirements that are used.

Figure 1 shows a reasonable agreement between simulations and experiments.³³ It is important to note here that numerical results of Figure 1 do not depend on any free or fitting parameters since our numerical calculations only require standard characteristics of liquid and gaseous water and the knowledge of boundary conditions. As the droplet is heated from below, it is important to note here that T_s and T_{∞} are different. In the following $T_s - T_{\infty} > 10\text{ }^{\circ}\text{C}$. We assumed that, in such conditions, evaporative mass flux at each point of the free surface are determined by the local heat flux that is itself ruled by temperature gradients. Still we verified that when T_s becomes close to T_{∞} , numerical outputs converge to the predictions of the analytical model developed in ref 14, where the evaporating droplet problem is mapped into an equivalent electrostatic model that can be solved analytically.

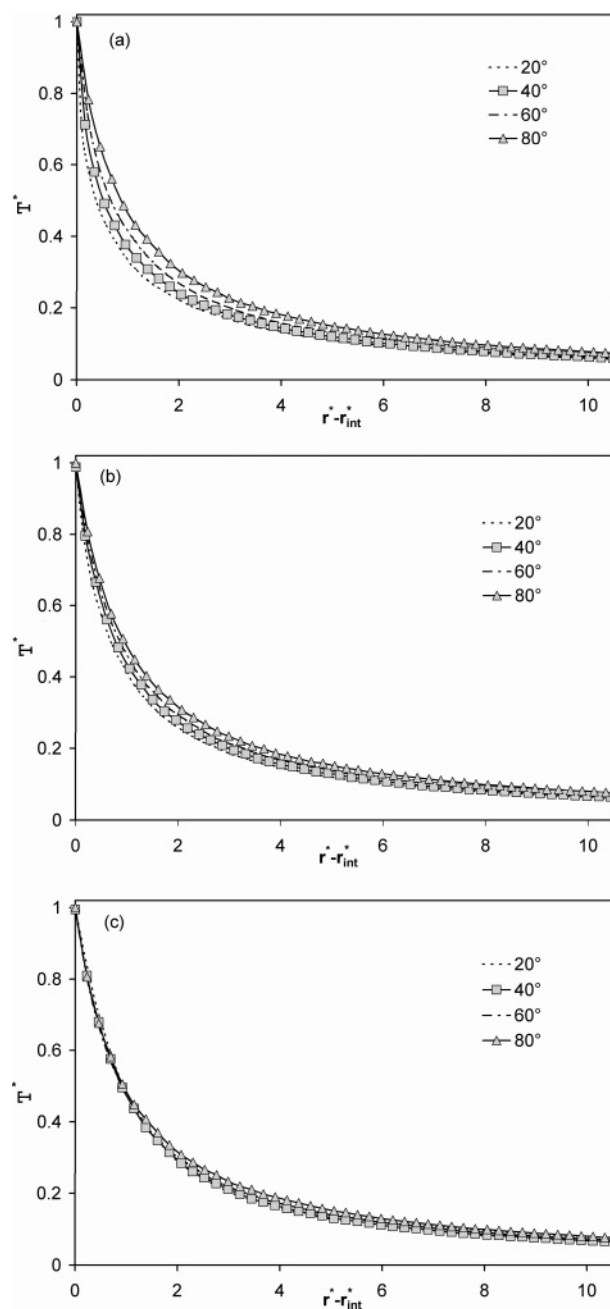


Figure 2. Temperature profile for $T_s = 60\text{ }^{\circ}\text{C}$ in the direction normal to the interface at the edge of the droplet $r^*_{\text{int}} = 1$ (a), at $r^*_{\text{int}} = 0.5$ (b), and at the apex of the droplet $r^*_{\text{int}} = 0$ (c).

This is based on the analogy between the diffusive vapor field and the electrostatic potential generated by a biconvex conducting lens.^{1,2,34,35}

As just mentioned, the evaporative flux along the interface depends on the temperature gradients in the surrounding air. As temperature gradients change from one point to the other, local evaporative mass flux is non-uniform. We introduce the dimensionless temperature T^* defined by $T^* = (T - T_{\infty})/(T_s - T_{\infty})$, where T is the true temperature and is denoted in the following by $r^* = r/R$, the normalized radius. The behavior of T^* in the normal direction of the free interface is shown for different contact angles and for different radial coordinates r^*_{int} in Figure 2 for a $R = 1\text{ mm}$ radius droplet. At the edge of the droplet (i.e., when

(33) Crafton, E. F.; Black, W. Z. *Int. J. Heat Mass Transfer* **2004**, *47*, 1187–1200.

(34) Lebedev, N. N. *Special Function and Their Applications*, Prentice-Hall: Englewood Cliffs, NJ, 1965.

(35) Picknett, R. G.; Bexon, R. J. *Colloid Interface Sci.* **1977**, *61*, 336.

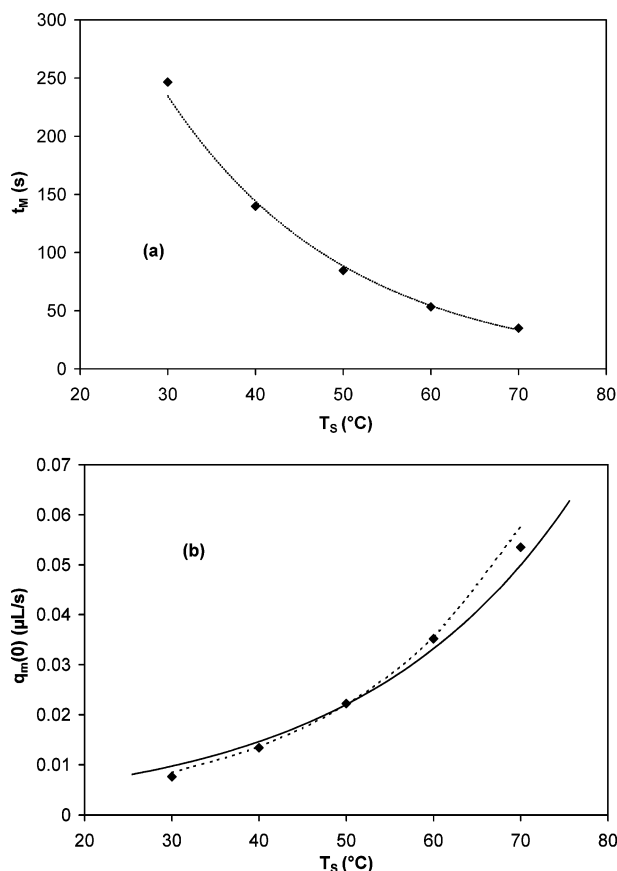


Figure 3. (a) Evaporation time t_M and (b) initial mass flow $q_m(0)$ as a function of the substrate temperature T_s for droplet radius $R = 1$ mm and initial contact angle of 80° . The dashed line in a (respectively b) corresponds to an exponential fitting $10^3 \exp(-4.8 \times 10^{-2} T_s)$ (respectively $2 \times 10^{-3} \exp(-4.8 \times 10^{-2} T_s)$). The full line in b corresponds to experimental data that were provided to us by Dr. K. Sefiane.³⁶

radial coordinate $r^*_{\text{int}} = 1$) Figure 2a shows increasing temperature gradients as the contact angle decreases. These gradients remain finite in the simulated contact angle range as long as $\theta > 10^\circ$. This indicates that the resulting evaporative mass flux rises at the droplet edge as the contact angle decreases but does not diverge. This is due to the free substrate temperature outside the droplet contact area. The temperature on the substrate outside the droplet is indeed freely determined by the Laplace equation and consequently leads to smooth normal temperature gradients everywhere on the droplet surface. Figure 2b corresponds to the normal temperature profile for $r^*_{\text{int}} = 0.5$ and shows temperature gradients that are smaller than at the edge but still show an increasing sharpness as the contact angle decreases. Finally at the apex of the droplet, normal temperature becomes almost independent of the contact angle, as illustrated in Figure 2c. Comparison of Figure 2a–c for a given value of θ shows increasing temperature gradients from the edge to the apex of the droplet. As for a given value of the contact angle, normal temperature gradients change; local evaporation flux is non-uniform along the free interface.

In the following we restrict presentation of the results to droplets having $R = 1$ mm radius. For such droplets, the total evaporation time t_M as a function of the heating temperature is given in Figure 3a. It indicates a rapidly decreasing behavior. For the simulations of Table 1, evaporation occurs for few seconds up to slightly more than 1 min. An exponential fitting of the data indicates that $t_M \approx 10^3 \exp(-4.8 \times 10^{-2} T_s)$ with good agreement. For temperatures between 30 and 70 °C the thermal diffusivity

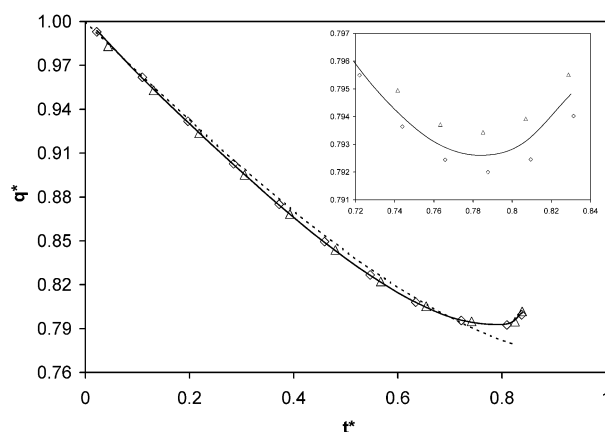


Figure 4. Evolution of the normalized mass flow $q^* = q_m(t)/q_m(0)$ as a function of the normalized time $t^* = t/t_M$ for substrate temperatures $T_s = 30$ (diamonds), 50 (full line), and 70 °C (triangles). The inset shows the detail of the curve in the minimum region. The dashed line corresponds to the time evolution $\Sigma(t^*)$.

of water is almost a linear function of temperature. This fast decreasing evolution of t_M is related to evaporating dynamics involving not only diffusive transport of heat across the droplet but also diffusion of water in the surrounding air. The initial mass flow $q_m(0)$ is obtained when contact angle $\theta \approx 80^\circ$. It is plotted in Figure 3b and shows an exponential increase with substrate temperature with a reasonable good agreement with experimental data.³⁶

The time evolution of the droplet volume for substrate temperature ranging from 30 to 70 °C shows very similar characteristics. The main result of the volume evolution is a clear nonlinear decrease that traduces in particular a slowing down of the mass flow as the evaporative process takes place.^{37,38} The time evolution of the normalized mass flow $q^* = q_m(t)/q_m(0)$ is shown in Figure 4 as a function of normalized time and for several heating temperatures. The use of normalized quantities makes possible an immediate comparison between the evaporating regimes generated by different substrate temperatures. The slowing down of evaporation appears clearly as a reduction of the mass flow that turns out to be larger than 20% of its initial value. One straightforward explanation relies on the fact that the interface surface decreases, and, hence, the available room for water to leave the droplet shrinks as the droplet evaporates. This reduction of the evaporating surface is not balanced by the rising of the droplet temperature or vapor gradient sharpening, and the resulting mass flow in the first evaporation phase decays. This decay is almost linear up to time $t^* \approx 0.4$, where $t^* = t/t_M$. A slowing down then appears, and $q_m(t)$ reaches a minimum value for $t^* \approx 0.78$, where the contact angle $\theta \approx 20^\circ$. Beyond this time $q_m(t)$ is ultimately rising. This nonconstant and nonlinear behavior of the mass flow can be qualitatively explained by the balance between the reduction of the effective surface of the free interface and the increasing interface temperature of the droplet. To this end, we follow the time evolution of $\Sigma(t^*) = (s(t^*)/s(0))^{1/2}$, where $s(t^*)$ is the interface surface at time t^* . Figure 4 shows that q^* and Σ have a similar time behavior as long as $t^* < 0.78$. This qualitative good agreement indicates that evaporative mass flow reduction is mainly due to the progressive surface decrease of the droplet. For $0.4 < t^* < 0.78$ both surface reduction and increasing droplet temperature effects start to compete, but $q_m(t)$

(36) Sefiane, K. *J. Pet. Sci. Eng.* **2006**, *51*, 238–252.

(37) Girard, F. Master degree, Université Paul Cézanne, Marseille, France, 2002.

(38) Girard, F.; Antoni, M.; Faure, S.; Steinchen, A. *Microgravity Sci. Technol.* **2006**, *18* (3/4), 42–46.

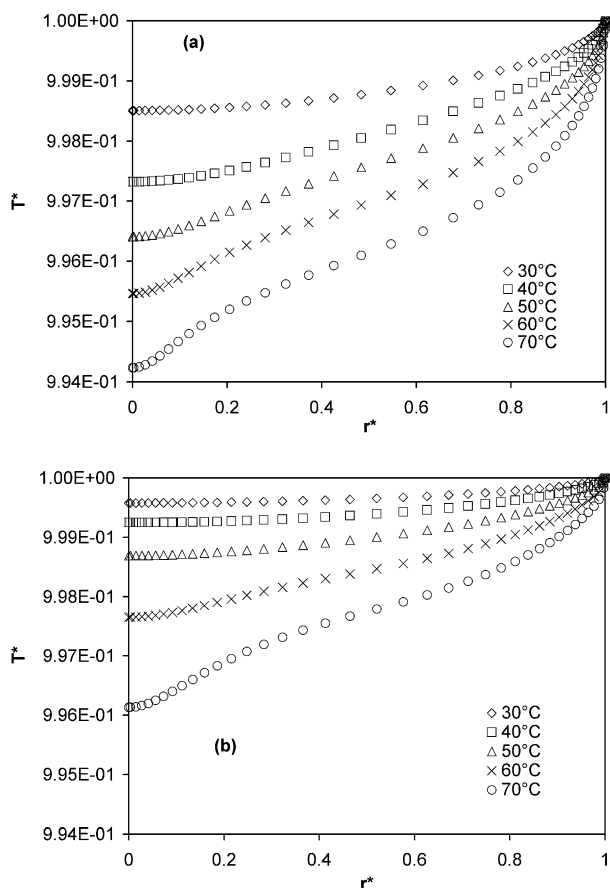


Figure 5. Normalized temperature T^* along the droplet interface as a function of the dimensionless radial coordinate r^* for different values of substrate temperature T_s , for $T_\infty = 20^\circ\text{C}$ and $H = 20\%$. $r^* = 0$ is the apex of the droplet. Panel a indicates temperature profiles for contact angle $\theta \approx 70^\circ$ and b for $\theta \approx 30^\circ$. Substrate temperatures are given by the symbols in the graphs.

and Σ still have similar behavior. For $r^* > 0.78$, however, the flow is enhanced due to the rising interface temperature and resulting rising gradients of vapor concentration in air.

The radial temperature changes along the interface are illustrated in Figure 5 and display the value of the nondimensional temperature T^* as a function of the dimensionless radius r^* for contact angle $\theta \approx 70^\circ$ and $\theta \approx 30^\circ$. Dimensionless temperature T^* is defined by $T^* = (T - T_\infty)/(T_s - T_\infty)$. In the following, we denote by r^* (instead of r as in eqs 1–6) the normalized radius. These figures show that the temperature is non-uniform on the water/air interface as already observed in refs 19 and 20. Due to cooler surrounding air, the droplet interface takes smaller temperature at its apex than elsewhere and in particular at the contact line level. Still, temperature differences between contact line and apex are small²⁰ and depend not only on the substrate temperature but also on the contact angle. Figure 5b shows, for example, that for $\theta \approx 30^\circ$, temperature differences range between $2 \times 10^{-1}^\circ\text{C}$ (for $T_s = 70^\circ\text{C}$) and $5 \times 10^{-3}^\circ\text{C}$ (for $T_s = 30^\circ\text{C}$). These results are consistent with previous numerical results.²⁰ Hence the temperature difference on the interface is much smaller than the difference $T_s - T_\infty$ between the substrate temperature and the one far apart from the droplet. These results differ significantly from the ones of ref 19.

The comparison of Figure 5a,b for a given value of T_s shows an increasing interface average temperature as contact angle drops. Consequently, due to temperature continuity across the interface, the air in the neighborhood of the droplet becomes warmer as the contact angle decreases and hence supports larger vapor

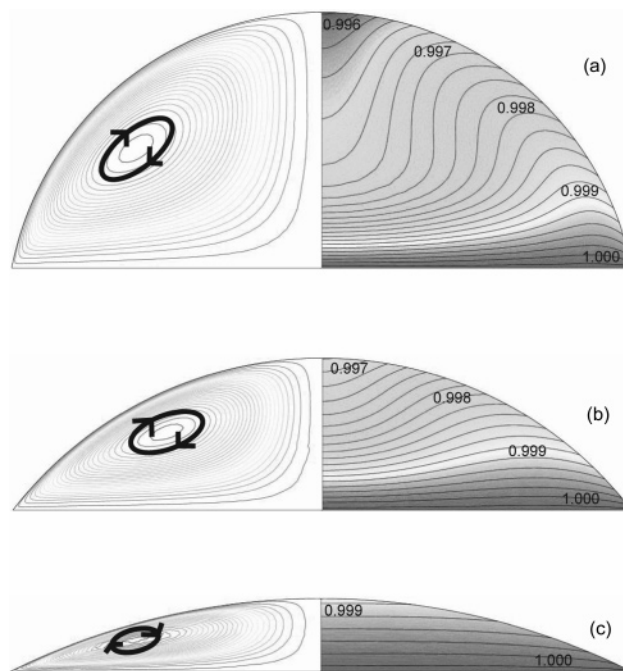


Figure 6. Streamlines (left) and isotherms (right) in the droplet for $T_s = 60^\circ\text{C}$ and $\theta = 80$ (a), 50 (b), and 20° (c). Black thick lines illustrate the course of the velocity field. Some values of T^* are indicated in the figures.

pressures. The latter increase with temperature³² and modify in turn vapor concentration profiles.

Temperature differences on free fluid interfaces are known to generate Marangoni stresses and a velocity flow that will drag the fluid from the warm regions, where surface tension is small, to the cold regions, where surface tension is larger. Due to the conservative and noncompressible properties of water, this velocity flow acts like a shear that will trigger convection motion inside the volume of the droplet.^{3,19,20,37,38} A recent numerical approach including non-uniform substrate temperature indicates also temperature inversions for contact angles smaller than 14° corresponding to situations where the droplet temperature is larger at its apex than at the contact line level.²⁰

Temperature profile and streamlines displayed in Figure 6 confirm the small temperature gradients but with a more distorted temperature field at $r^* = 0$ for large contact angles. It also illustrates the time dependence of temperature and velocity as evaporation takes place. As discussed previously temperature changes are comparatively small as contact angle decreases. Figure 7 indicates, however, that important changes can appear in the evolution of the velocity field along the interface when changing the value of T_s . These 3D plots show the Marangoni velocities $v^* = v/v_{\max}$, where $v = (u_r^2 + u_z^2)^{1/2}$ is the computed velocity modulus and v_{\max} its maximal value for each computed contact angles. Figure 7a corresponds to $T_s = 30^\circ\text{C}$ and shows a velocity field that keeps constant shape with a maximal value located in the vicinity of $r^* \approx 0.7$. This maximum is linked to the location of the convection cell that remains to an almost fixed position as evaporation takes place. For $T_s = 60^\circ\text{C}$, Figure 7b displays a more complex situation. For large contact angles, the velocity is again maximal in the vicinity of $r^* \approx 0.7$ but, as θ decreases, the maximal velocity location progressively shifts toward the apex of the droplet ($r^* \approx 0.3$ for $\theta = 50^\circ$) before drifting back to the contact line ($r^* \approx 0.6$ for $\theta = 20^\circ$). A similar swinging effect was already present in Figure 7a but with a smaller amplitude. This phenomenon actually shows up for all the simulations with amplitude increasing with T_s .

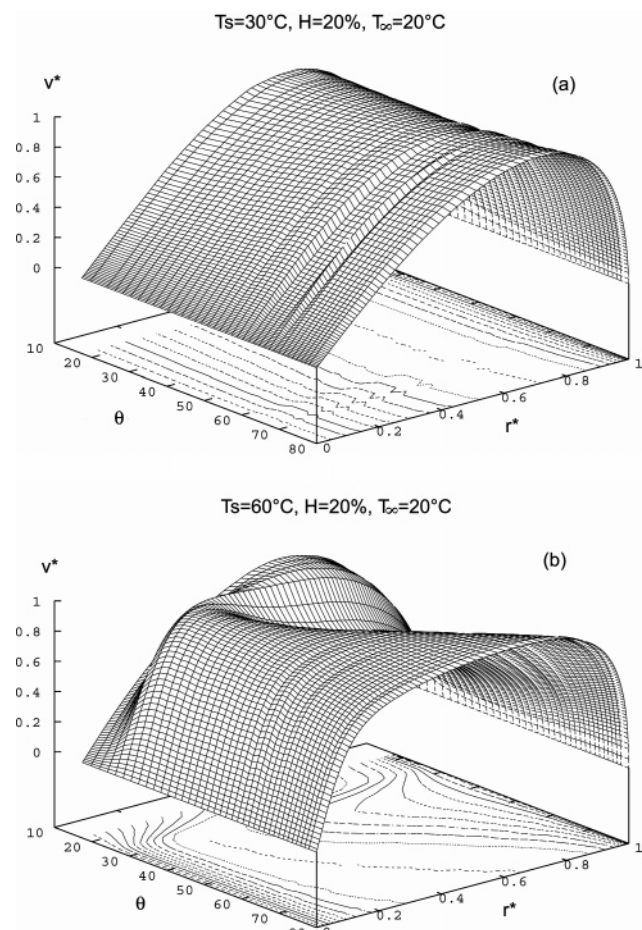


Figure 7. 3D plot of the velocity v^* on the free interface as a function of r^* and contact angle θ at temperature $T_s = 30$ (a) and 60 °C (b). Contour lines of the surface are also plotted.

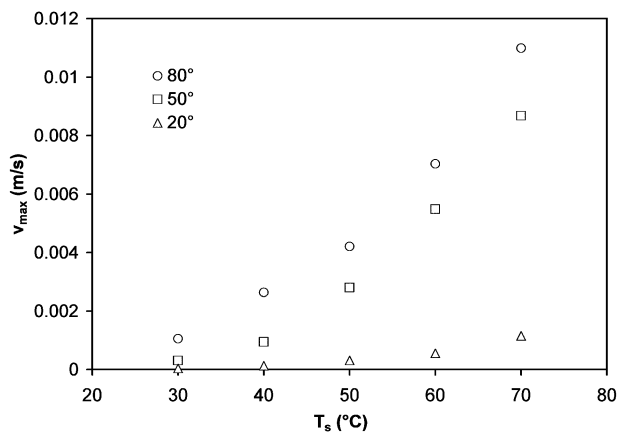


Figure 8. Maximal velocity v_{\max} on the interface as a function of substrate temperature T_s . Circles, squares, and triangles correspond respectively to contact angles $\theta = 80$, 50 , and 20 °.

The shape of the Marangoni velocity field is linked to the position of the center of the convective cell that drifts from $r^* \approx 0.6$ for $\theta = 80^\circ$ to $r^* \approx 0.5$ for $\theta = 50^\circ$ and back to $r^* \approx 0.6$ for $\theta = 20^\circ$. We believe this fluctuating effect might play a fundamental role on the deposited microparticle patterns observed in experiments. Convective motions indeed dominate particle diffusion and hence determine the deposition pattern.²⁰ But if the convective cells, beside the usual oscillating dynamics,

also exhibit global motion of their center as evaporation goes on, the resulting deposited profiles might be strongly modified.

The maximal velocity v_{\max} of the Marangoni field used in the plots of Figure 7 is displayed in Figure 8 as a function of substrate temperature T_s and for several contact angles. For given T_s , v_{\max} decays to zero when contact angles fall due to diminishing temperature gradients along the interface as time evolves. Similarly, for a given contact angle, v_{\max} is lessening as T_s becomes close to T_∞ . Still, it is important to note here that the typical values of v_{\max} obtained from the simulations are of the order of a few millimeters per second. For example, when $T_s = 60$ °C, $v_{\max} = 7.0 \times 10^{-3} \text{ m}\cdot\text{s}^{-1}$ if $\theta = 80^\circ$, whereas $v_{\max} = 4.5 \times 10^{-3} \text{ m}\cdot\text{s}^{-1}$ when $\theta = 50^\circ$, and finally $v_{\max} = 5 \times 10^{-4} \text{ m}\cdot\text{s}^{-1}$ when $\theta = 20^\circ$. Hence hydrodynamics that develops inside the droplet will generate convective cells with characteristic frequency that range between several hertz down to fractions of hertz. Since evaporation time $t_M \approx 53$ s when $T_s = 60$ °C (see Figure 3a); an important number of oscillations can occur before complete evaporation of the droplet. Hence, convective motions cannot be considered here as negligible or as a transient phenomenon. This naturally raises the problem of viscous dissipation contributions that are not included in the model we investigate. Several tests were performed to precisely estimate their weight in the time evolution of the droplet. None of them produced changes larger than 1% in the results presented herein.

4. Conclusion

Numerical simulations of small evaporating sessile droplets show a nonlinear evolution of the droplet mass flow that results from the balance between the falling interface surface and its rising temperature due to heating substrate nearness. The evaporation time t_M is deduced from the time evolution of the contact angle and shows an exponential decaying behavior with increasing substrate temperatures. The study of the local temperature profile on the interface shows temperature gradients that create a Marangoni stress. The latter induces convective phenomena inside the droplet. The time evolution of the mass flow shows that evaporation regimes are qualitatively the same when the heating temperature is changed. It exhibits a minimum for contact angle $\theta \approx 20^\circ$ resulting from the crossing over between two evaporating regimes that are first ruled by the decreasing interface surface and then by thermal effects in both the droplet and surrounding vapor. The main consequence of this observation is the demonstration of the existence of several evaporating regimes in sessile droplet situations. This article also raises the problem of convective phenomena in small objects under microgravity conditions. Temperature gradients generate convective phenomena with a relative high frequency even for droplets that have radius $R = 1$ mm. The existence of convective cells and their drifting motion as evaporation goes on demonstrates that heat transport is ruled by mechanisms more complex than diffusive regimes. We believe that they constitute key phenomena for the understanding of evaporation dynamics and in particular pattern formation after total evaporation of droplets containing solid suspensions.

Acknowledgment. The authors gratefully acknowledge D. Fougère and B. Roux for their important support setting up programs and computer power. The authors also thank D. Veyret for determinant seminal discussions and computational help.

LA061572L